PNAS

1

Supporting Information for

Observed humidity trends in dry regions contradict climate models

Isla R Simpson, Karen A. McKinnon, Daniel Kennedy, David M. Lawrence, Flavio Lehner, and Richard Seager

Corresponding Author Isla Simpson.
E-mail: islas@ucar.edu

This PDF file includes:

Table S1. Summary of CMIP6 model simulations used.

Model	# members
ACCESS-CM2	3
ACCESS-ESM1-5	5
AWI-CM-1-1-MR	1
BCC-CSM2-MR	1
CanESM5	5
CAS-ESM2-0	2
CESM2-WACCM	3
CMCC-CM2-SR5	1
CMCC-ESM2	1
CNRM-CM6-1	5
CNRM-CM6-1-HR	1
CNRM-ESM2-1	5
E3SM-1-1	1
E3SM-1-1-ECA	1
EC-Earth3	8
EC-Earth3-Veg	8
EC-Earth3-Veg-LR	3
FGOALS-f3-L	1
FGOALS-g3	4
FIO-ESM-2-0	3
GFDL-CM4	1
GFDL-ESM4	1
GISS-E2-1-G	5
GISS-E2-1-H	5
HadGEM3-GC31-LL	4
HadGEM3-GC31-MM	4
IITM-ESM	1
INM-CM4-8	1
INM-CM5-0	1
IPSL-CM6A-LR	7
KACE-1-0-G	3
KIOST-ESM	1
MIROC6,50	1
MIROC-ES2L	10
MPI-ESM1-2-HR	2
MPI-ESM1-2-LR	30
MRI-ESM2-0	5
NorESM2-LM	1
NorESM2-MM	1
TaiESM1	1
UKESM1-0-LL	5

Table S2. Summary of AMIP6 model simulations used.

Model	# members
ACCESS-CM2	4
ACCESS-ESM1-5	10
CanESM5	2
CAS-ESM2-0	4
CESM2-WACCM	3
CMCC-CM2-SR5	1
CMCC-CM2-HR4	1
CNRM-CM6-1	1
CNRM-CM6-1-HR	1
CNRM-ESM2-1	1
E3SM-1-0	3
E3SM-2-0	3
EC-Earth3	6
EC-Earth3-Veg	3
EC-Earth3-Veg-LR	1
FGOALS-f3-L	3
FGOALS-g3	3
GFDL-ESM4	1
GISS-E2-1-G	5
HadGEM3-GC31-LL	5
HadGEM3-GC31-MM	4
IITM-ESM	1
INM-CM4-8	1
INM-CM5-0	1
IPSL-CM6A-LR	22
KACE-1-0-G	1
KIOST-ESM	1
MIROC6	10
MIROC-ES2L	3
MPI-ESM1-2-HR	3
MPI-ESM1-2-LR	3
MRI-ESM2-0	3
NorESM2-LM	1
TaiESM1	1
UKESM1-0-LL	1

Table S3. Summary of CMIP5 model simulations used.

Model	# members
ACCESS1-0	1
ACCESS1-3	1
bcc-csm1-1	1
bcc-csm1-1-m	1
BNU-ESM	1
CanESM2	5
CCSM4	6
CESM1-BGC	1
CESM1-CAM5	3
CESM1-WACCM	3
CNRM-CM5	5
CSIRO-Mk3-6-0	10
FGOALS-g2	1
FIO-ESM	3
GFDL-CM3	1
GFDL-ESM2G	1
GFDL-ESM2M	1
GISS-E2-H	2
GISS-E2-H-CC	1
GISS-E2-R	2
GISS-E2-R-CC	1
inmcm4	1
IPSL-CM5A-LR	4
IPSL-CM5A-MR	1
IPSL-CM5B-LR	1
MIROC5	2
MIROC-ESM	1
MIROC-ESM-CHEM	1
MRI-CGCM3	1
MRI-ESM1	1
NorESM1-M	1
NorESM1-ME	1

Isla R Simpson, Karen A. McKinnon, Daniel Kennedy, David M. Lawrence, Flavio Lehner, and Richard Seager
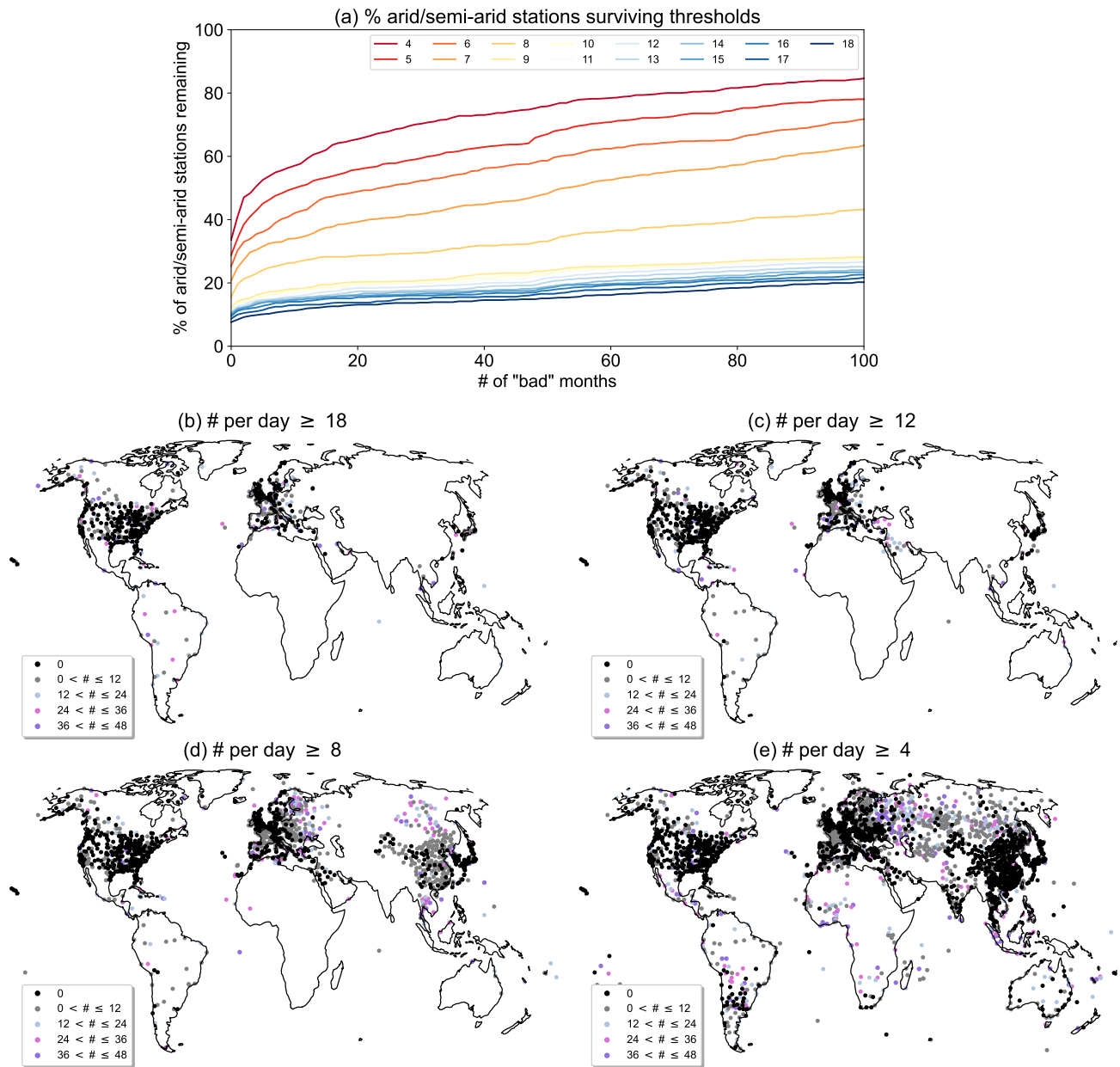
Fig. S1. An assessment of the data availability for the ISD stations used in this study. Defining "bad days" as days that have less than N quality observations and "bad months" as months where more than 15 days in the month are bad days, panel (a) shows the percentage of stations in arid/semi-arid regions that have have less than or equal to the number of bad months on the x-axis, for different N's depicted by the colors. Panel (b) shows the stations that have more than 18 observations per day and less than 48 bad months in the record with color coding of the dots indicating the number of bad months as given by the legend. (c)-(e) are as (b) but for N=12, 8 and 4 per day respectively.
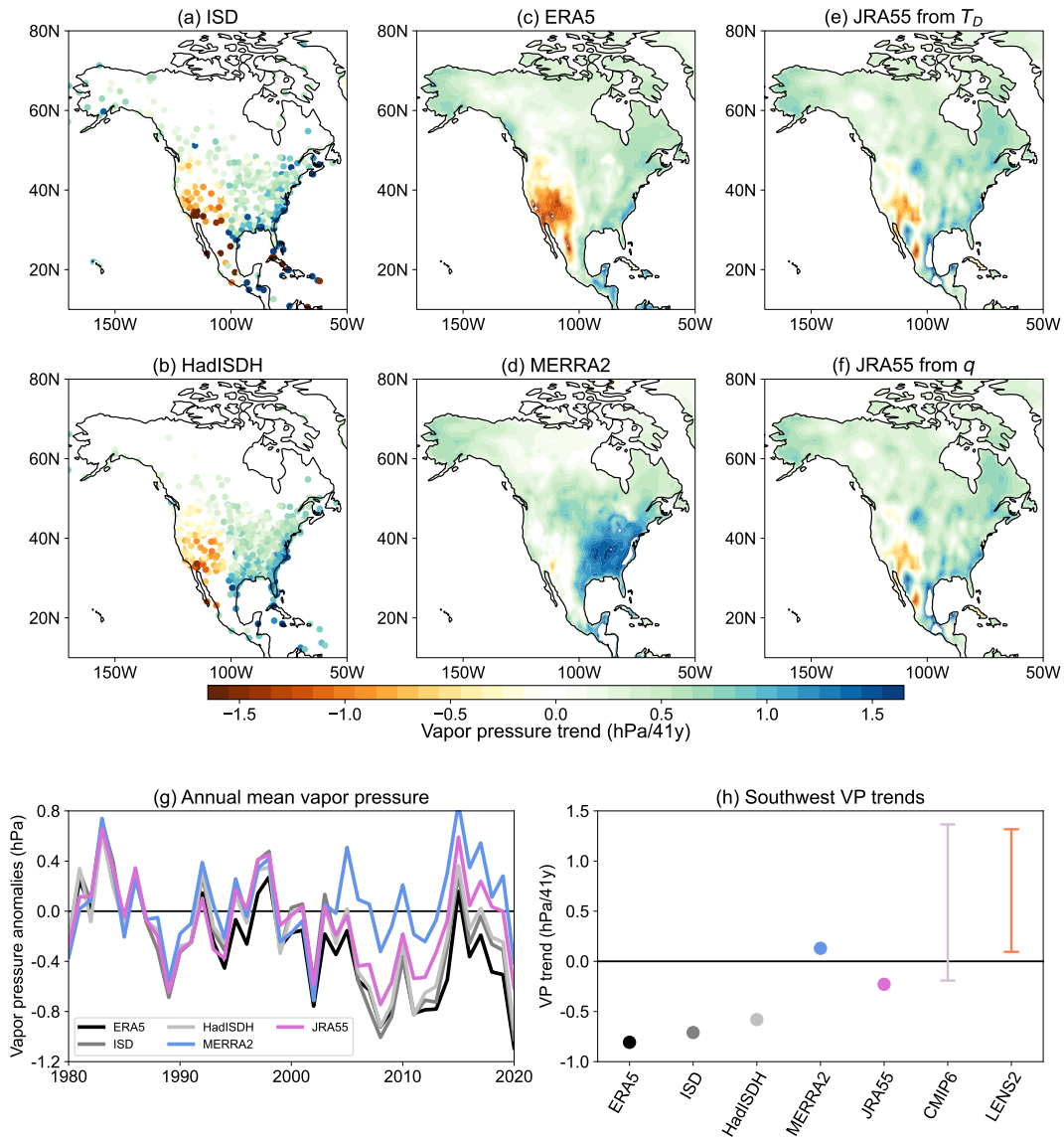
Fig. S2. (a)-(f) show annual mean vapor pressure trends from 1980 to 2020 over North America for ISD, HadISDH, ERA5, MERRA2, JRA55 calculated from dew point temperature, and JRA55 calculated from specific humidity at 2 m, respectively. (g) shows time series of annual mean vapor pressure averaged over the 6 states of the Southwest (using the dew point version for JRA55). (h) A comparison of the 1980 to 2020 trends averaged over the Southwest between reanalyses and the CMIP6 and LENS2 model ranges.
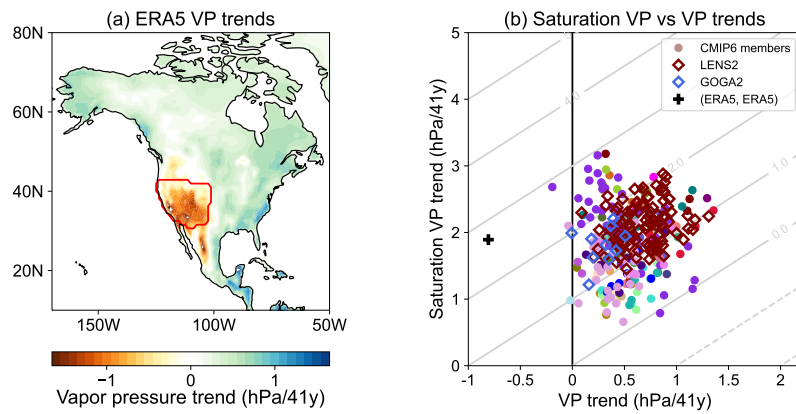
(a) ERA5 VP trends

(b) Saturation VP vs VP trends

Fig. S3. (a) is as Fig. 1b of the main text and (b) is as Fig. 1c of the main text but using the climatological surface pressure for each month of the year in the VP calculation.
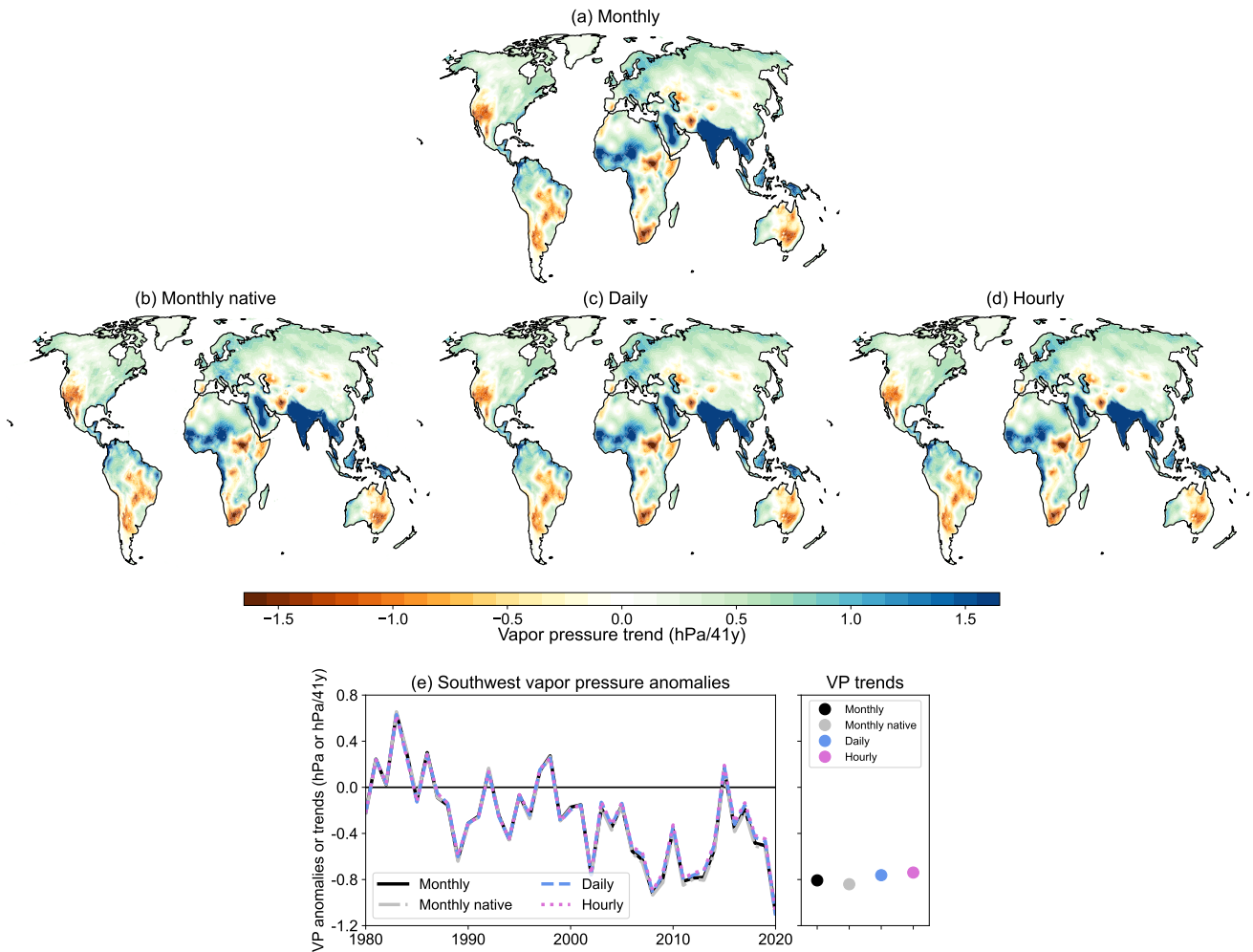
Fig. S4. 1980 to 2020 trends in annual mean vapor pressure from ERA5 calculated using (a) monthly averaged dew point temperature on the ∼1° grid (as in the main text), (b) monthly averaged dew point temperature on the native ERA5 grid, (c) daily averaged dew point temperature on the ∼1° grid, or (d) hourly instantaneous dew point temperature on the ∼1° grid. (e) shows the time series of annual mean vapor pressure (left) and the 1980 to 2020 trends averaged over the US Southwest calculated using monthly averaged, monthly averaged on the native grid, daily averaged, and hourly instantaneous dew point temperature.
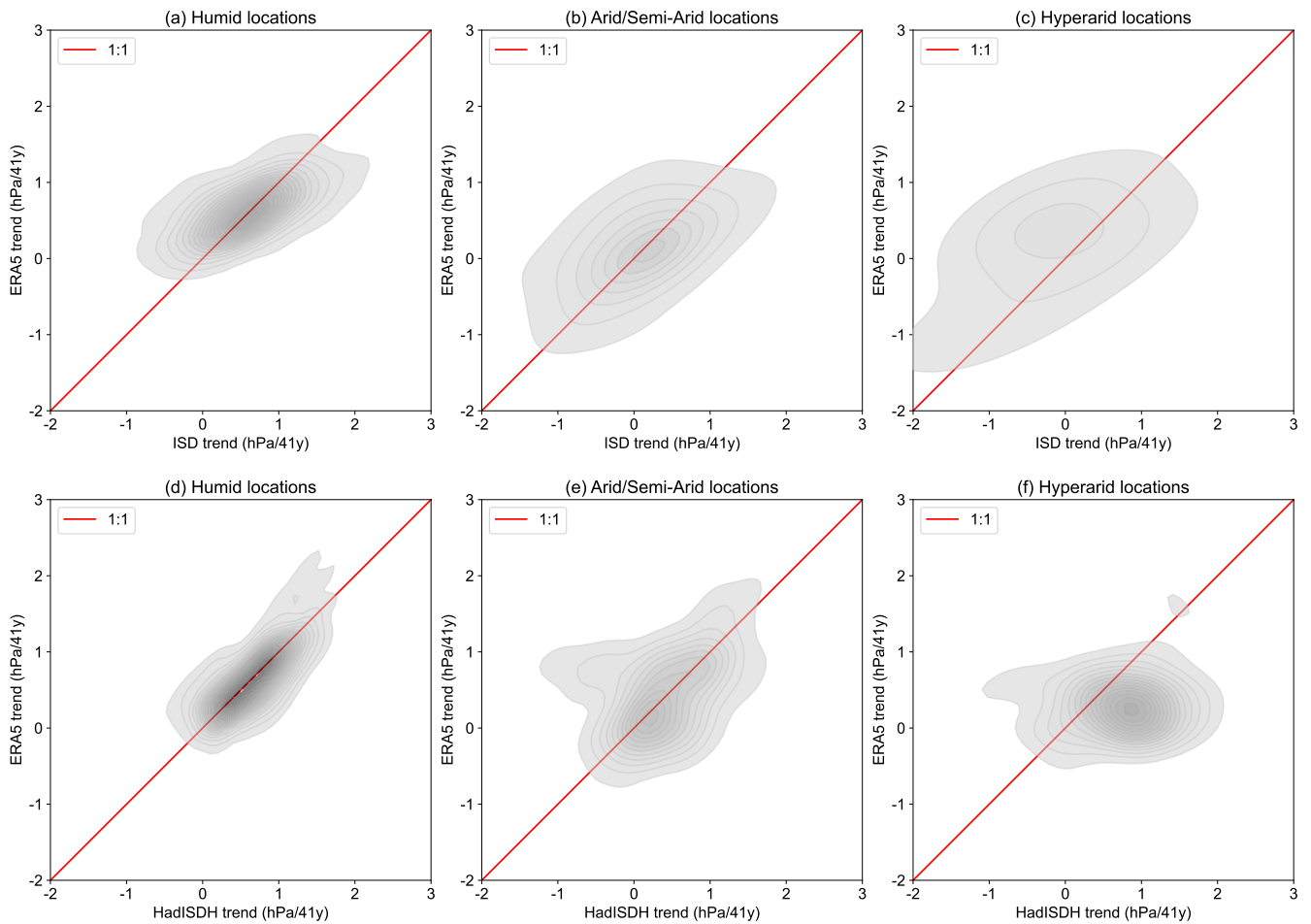
Fig. S5. Joint probability kernel density estimate of ERA5 vapor pressure trends (y-axis) and station-based vapor pressure trends (x-axis) for (top) ISD and (bottom) HadISDH. The stations are being compared with the closest ERA5 grid point on the 0.25° longitude by 0.25° latitude grid. Contours show the probability in % per 0.1 hPa/41y by 0.1 hPa/41y grid box, with contouring starting at 0.05% and increasing in increments of 0.05%. (a) and (d) show stations in humid locations, (b) and (e) show stations in arid/semi-arid locations and (c) and (f) show stations in hyperarid locations.
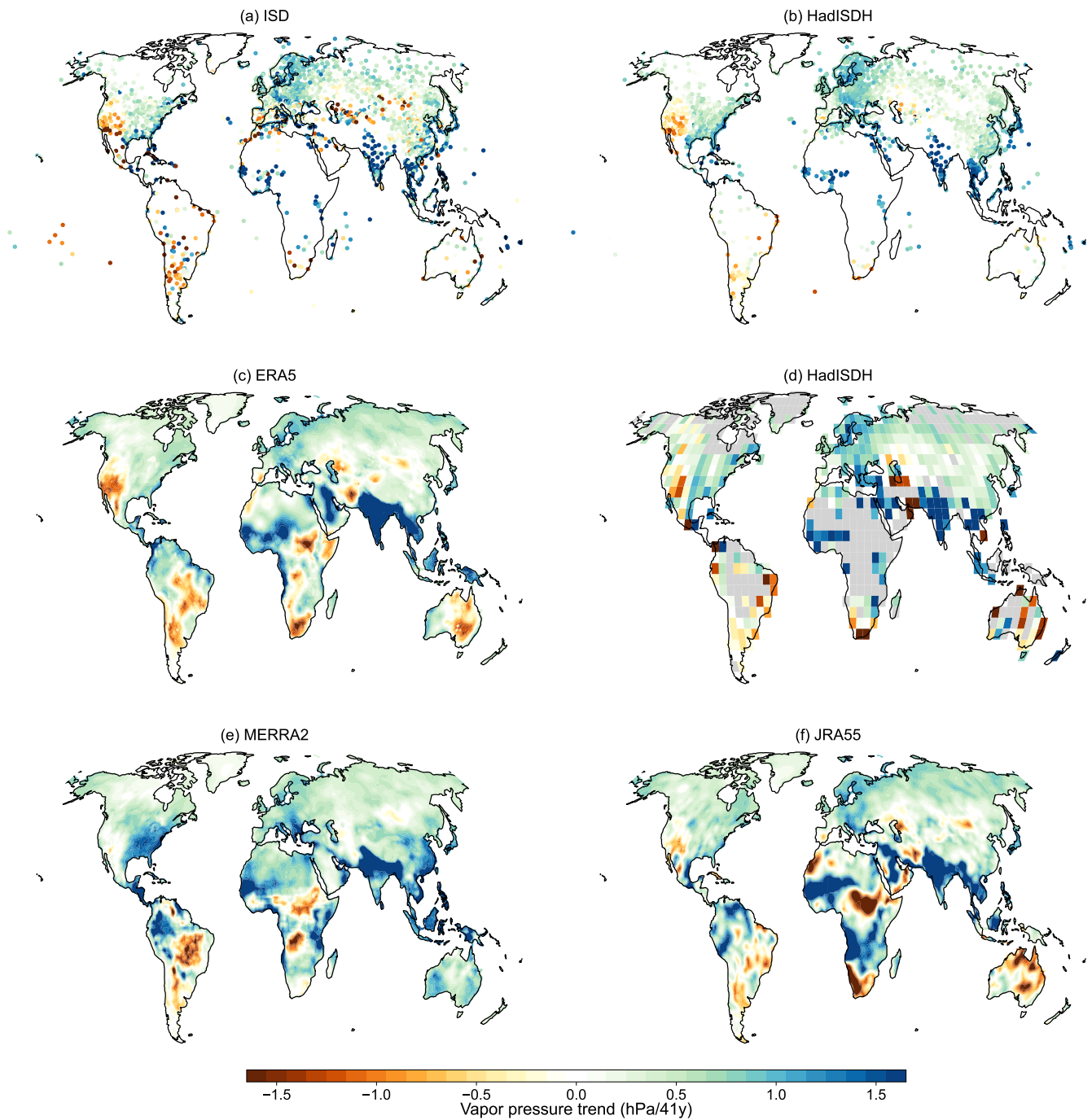
Fig. S6. 1980 to 2020 trends in annual mean vapor pressure for (a) ISD, (b) HadISDH, (c) ERA5, (d) the HadISDH gridded product, (e) MERRA2, and (f) JRA55.
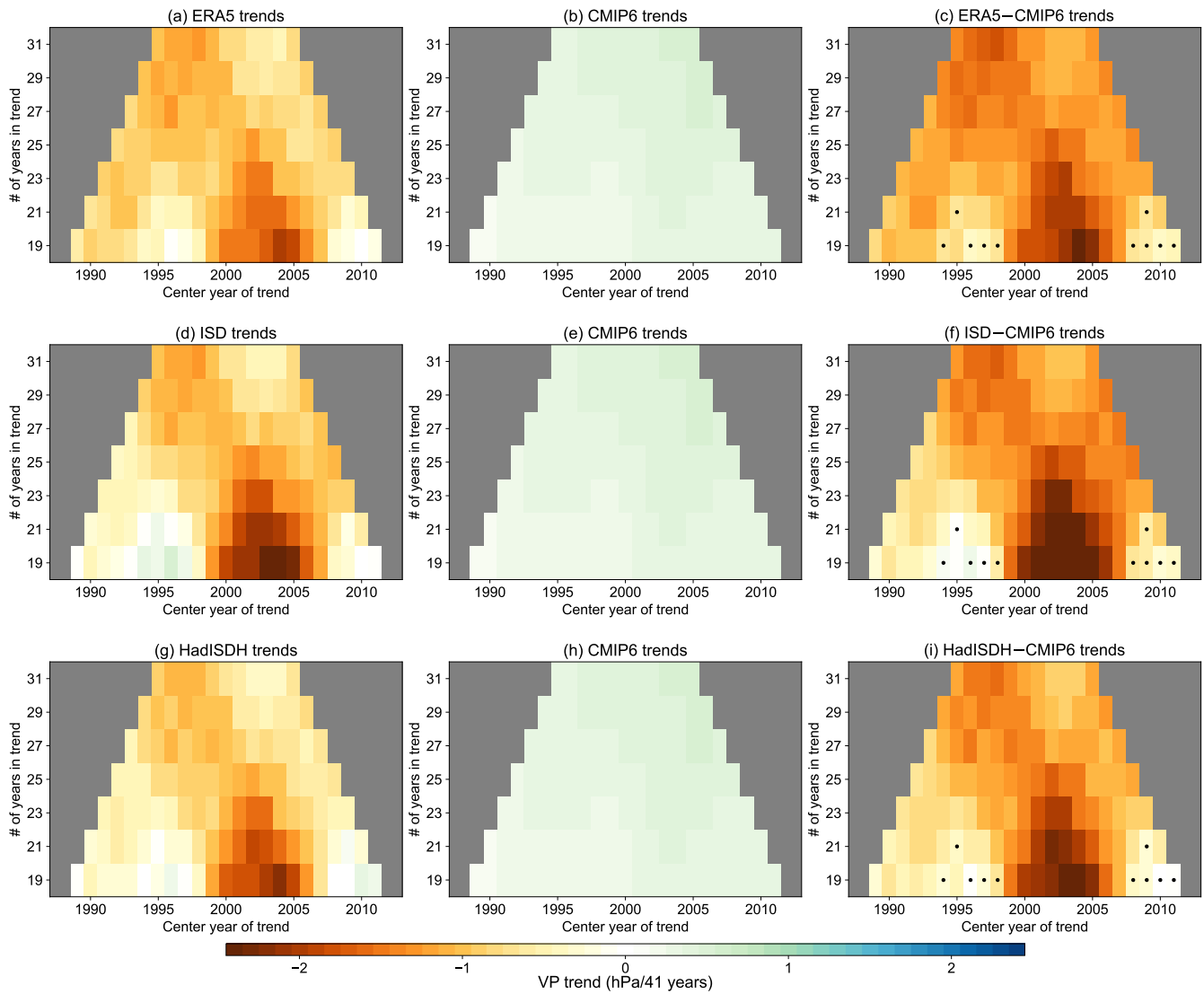
Fig. S7. Rolling trends of annual mean vapor pressure over the Southwest of length given by the y-axis, centered on the year given by the x-axis. (a) ERA5 trends, (b) ensemble mean of CMIP6 trends, (c) the difference between ERA5 and the CMIP6 ensemble mean with dots showing where the ERA5 trends lie within the 2.5th to 97.5th percentile range of CMIP6 ensemble members. (d)-(f) are as (a)-(c) but using the ISD station Southwest average for the observed dataset and (g)-(i) are as (a)-(c) but using the HadISDH stations as the observed dataset.
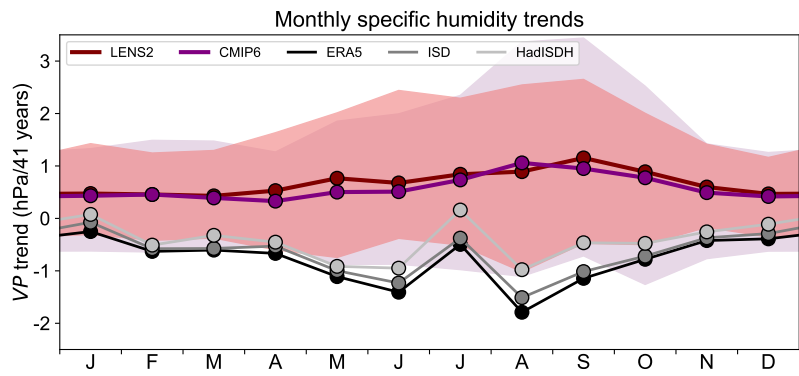
Fig. S8. As Fig. 1g of the main text but showing the VP trend in hPa per 41 years as opposed to in percent of the 1980 to 1990 climatology per 41 years.
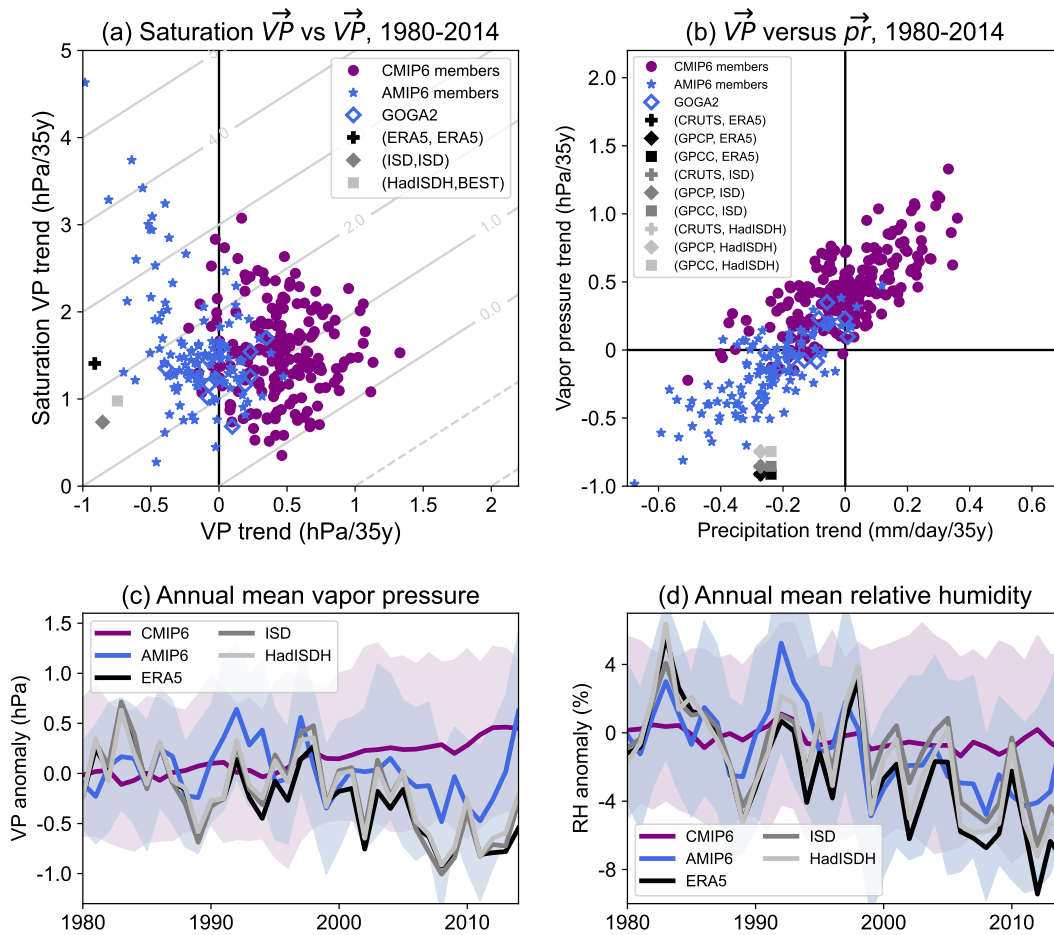
Isla R Simpson, Karen A. McKinnon, Daniel Kennedy, David M. Lawrence, Flavio Lehner, and Richard Seager

(a) Saturation $\overrightarrow{VP}$ vs $\overrightarrow{VP}$, 1980-2014

(b) $\overrightarrow{VP}$ versus $\overrightarrow{pr}$, 1980-2014

(c) Annual mean vapor pressure

(d) Annual mean relative humidity

Fig. S9. Trends from 1980 to 2014 over the US Southwest. Panel (a) is as Fig. 1c of the main text and shows saturation vapor pressure trend versus vapor pressure trend for all members from all models from CMIP6 (purple dots) and from all members from all models from AMIP6 (blue stars) along with the ERA5, ISD, and HadISDH trends. Panel (b) is as Fig. 2c of the main text and shows vapor pressure trend versus precipitation trend for all CMIP6 members (purple dots) and AMIP6 members (blue stars) as well as the observation-based datasets. (c) is as Fig. 1d of the main text and shows annual mean vapor pressure time series (anomalies from 1980-1990). Purple shows CMIP6 and the shading depicts the 2.5th to 97.5th percentile range across all members. Blue shows AMIP6 and the blue shading shows the 2.5th to 97.5th percentile range across all AMIP6 members. Black, dark gray, and light gray show ERA5, ISD, and HadISDH respectively. (d) is the same as (c) but for annual mean relative humidity.
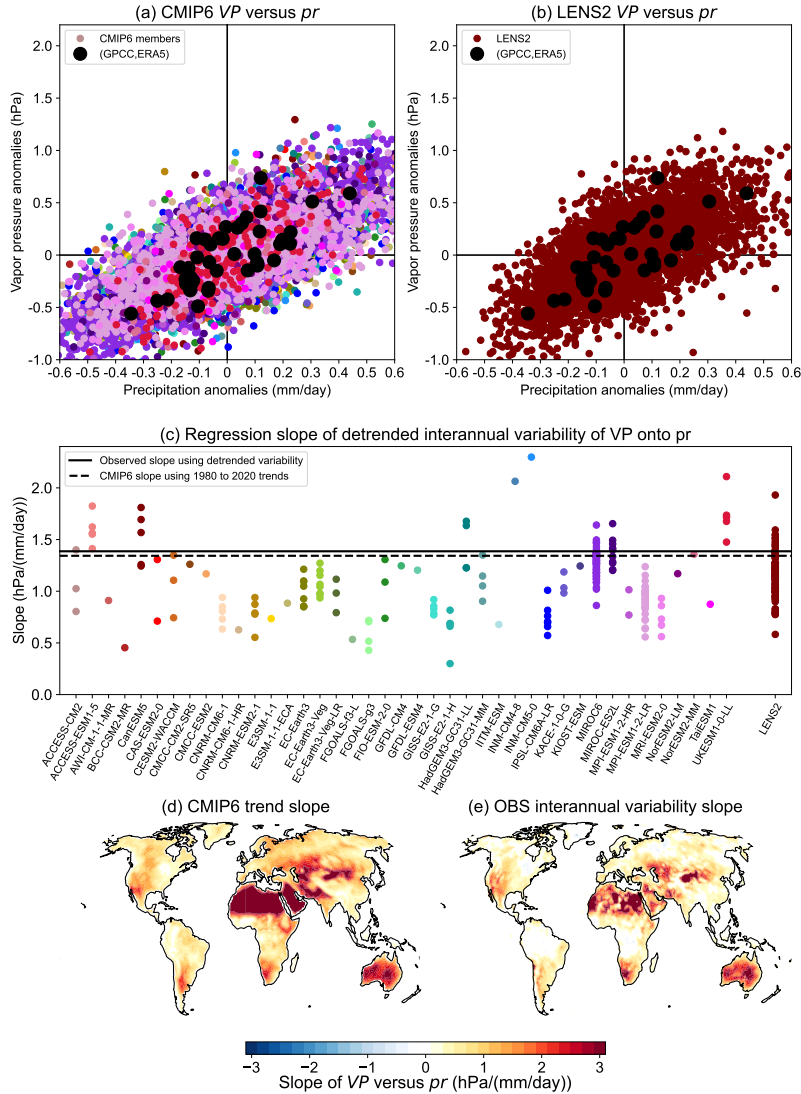
Fig. S10. The relationship between interannual variability in vapor pressure (VP) and precipitation (pr) over the 1980 to 2020 period after linearly detrending both VP and pr. (a) shows the relationship for the averages over the Southwest for each of the members of each of the CMIP6 models, with each CMIP6 model depicted by a different color, along with observation-based data in the large black dots. (b) is as (a) but for the CESM2 large ensemble members. (c) shows the slope of the regression of linearly detrended interannual variability of VP onto that of pr averaged over the Southwest for each of the CMIP6 models and LENS2, with the observation-based regression coefficient shown by the horizontal black line which can be compared with the horizontal dashed line which shows the regression slope of Fig 2a of the main text which uses 1980 to 2020 trends from the CMIP6 members. (d) Shows the slope of the regression across CMIP6 model members of 1980 to 2020 trends in VP onto 1980 to 2020 trends in pr i.e., the slope of the relationship [4] in the Methods of the main text. (e) shows the slope of the regression line of detrended interannal variability of ERA5 VP onto detrended interannual variability of GPCC pr.

Isla R Simpson, Karen A. McKinnon, Daniel Kennedy, David M. Lawrence, Flavio Lehner, and Richard Seager
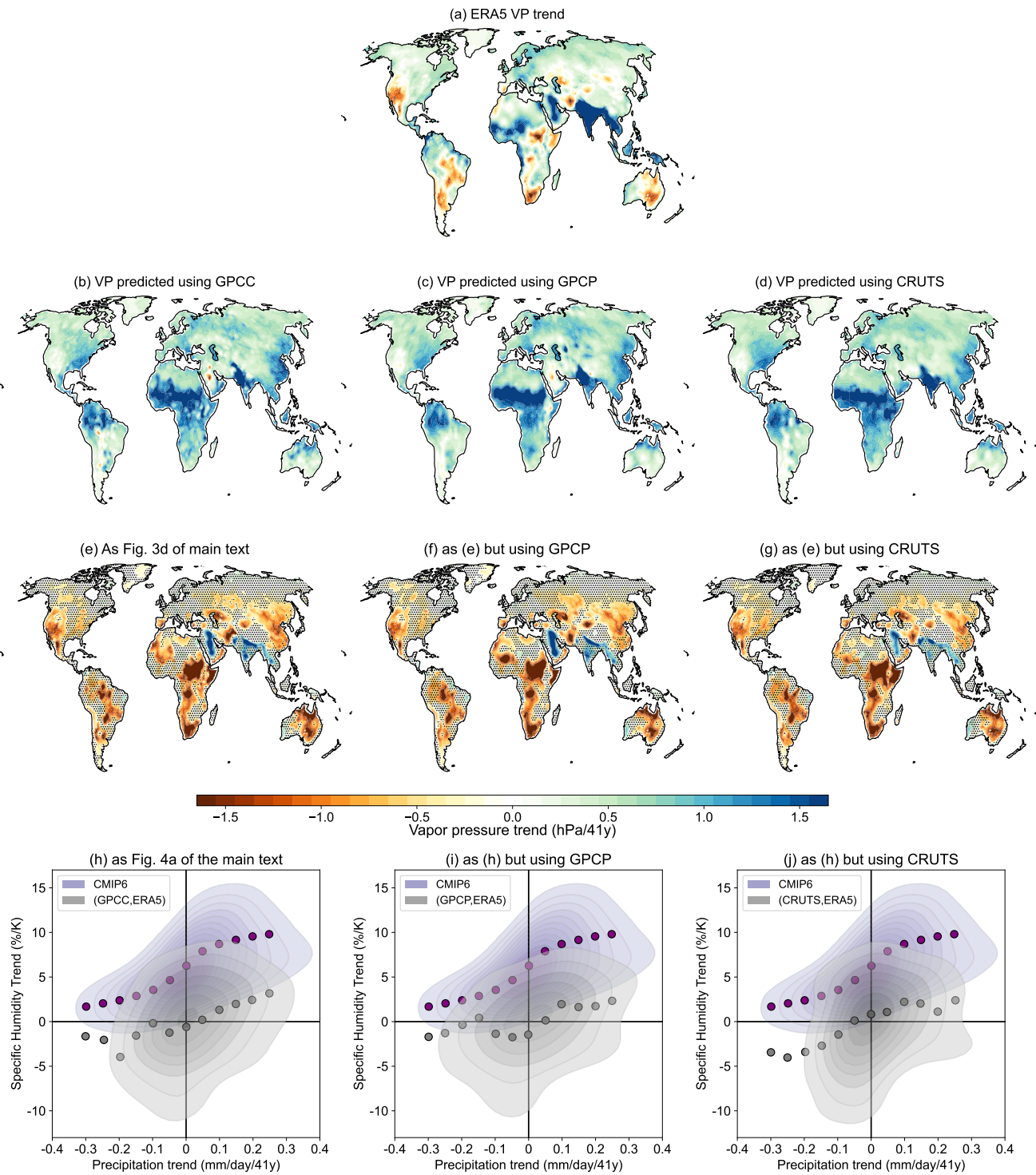
Fig. S11. (a) shows the 1980 to 2020 trend in annual averaged VP. (b)-(d) shows the vapor pressure trends predicted using the CMIP6 relationship between VP trend and precipitation trend and observed precipitation, using GPCC, GPCP, and CRUTS for the observed precipitation. (e)-(j) reproducing the main text figures that use GPCC but using the other precipitation datasets. (e) is a reproduction of Fig. 3d of the main text. (f) is as (e) but using GPCP for observed precipitation, and (g) is as (e) but using CRUTS for observed precipitation. (h) reproduces Fig. 4a of the main text and (i) and (j) are as (h) but using GPCP and CRUTS precipitation respectively.
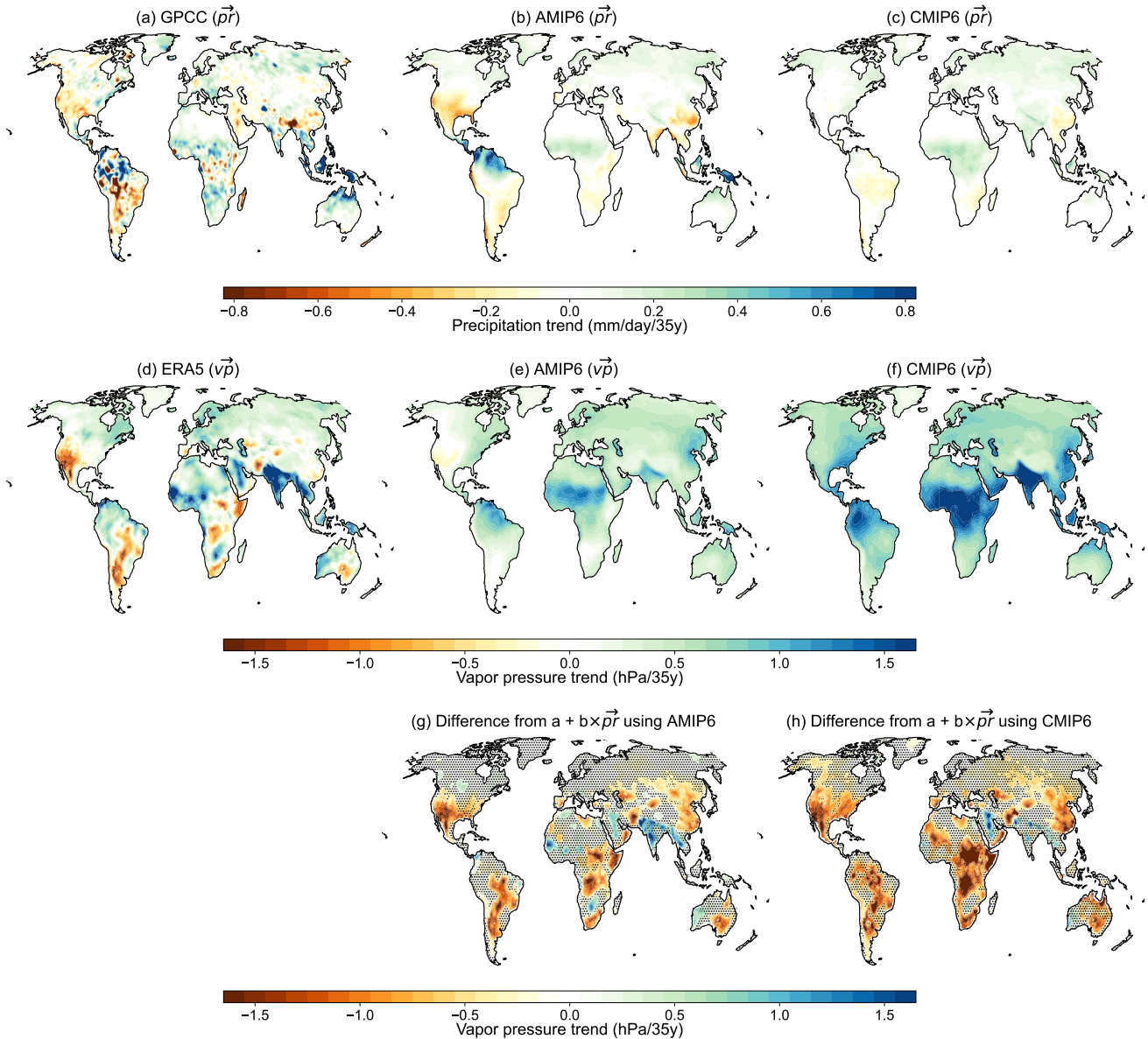
Fig. S12. Trends from 1980 to 2014. (a)-(c) annual mean precipitation trends for (a) GPCC, (b) the ensemble mean of the AMIP6 simulations, and (c) the ensemble mean of the CMIP6 simulations. (d)-(f) annual mean vapor pressure trends for (d) ERA5, (e) the AMIP6 ensemble mean, and (f) the CMIP6 ensemble mean. (g) shows the difference between the ERA5 vapor pressure trend and that predicted based on the linear relationship $\overrightarrow{VP} = a + b \times pr$ where a and b are determined at each grid point using the AMIP6 members and GPCC precipitation trends are used for observed precipitation i.e., this is equivalent to Fig 3d of the main text but using the 1979 to 2014 period and using the AMIP ensemble members. (h) is as (g) but using the CMIP6 members instead.
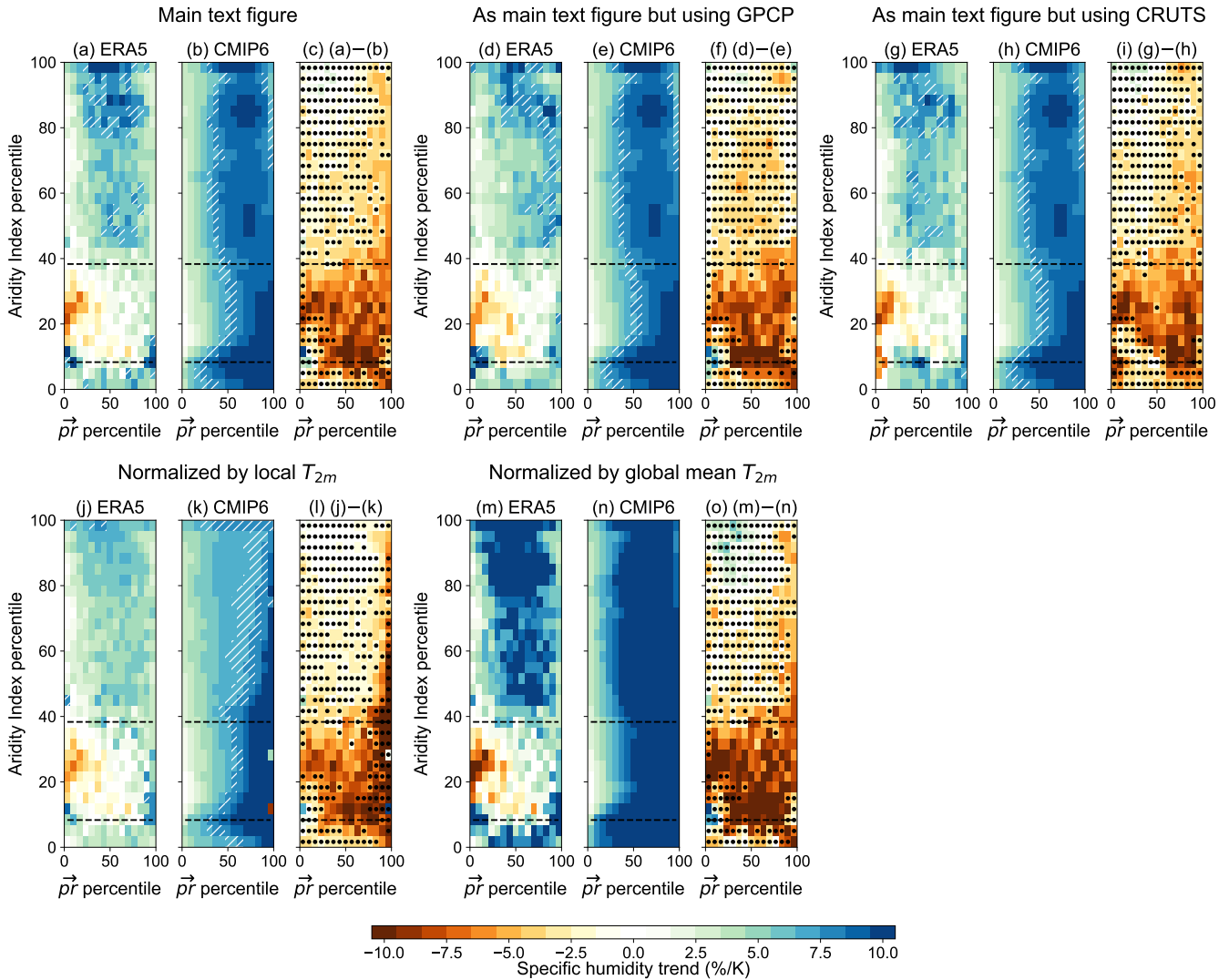
16 of 27   **Isla R Simpson, Karen A. McKinnon, Daniel Kennedy, David M. Lawrence, Flavio Lehner, and Richard Seager**

Fig. S13. Testing the sensitivity of Figs. 3h-j to the datasets and methods. (a)-(c) reproduces these panels of the main text which use GPCC to bin according to precipitation trend percentile. (d)-(f) are as (a)-(c) but using GPCP, (g)-(i) are as (a)-(c) but using CRUTS. In the main text, the specific humidity trends were normalized by the area averaged temperature trend over land and in (j)-(l) the trends are instead normalized by the bin mean temperature trend and in (m)-(o) they are normalized by the full global mean temperature trend.
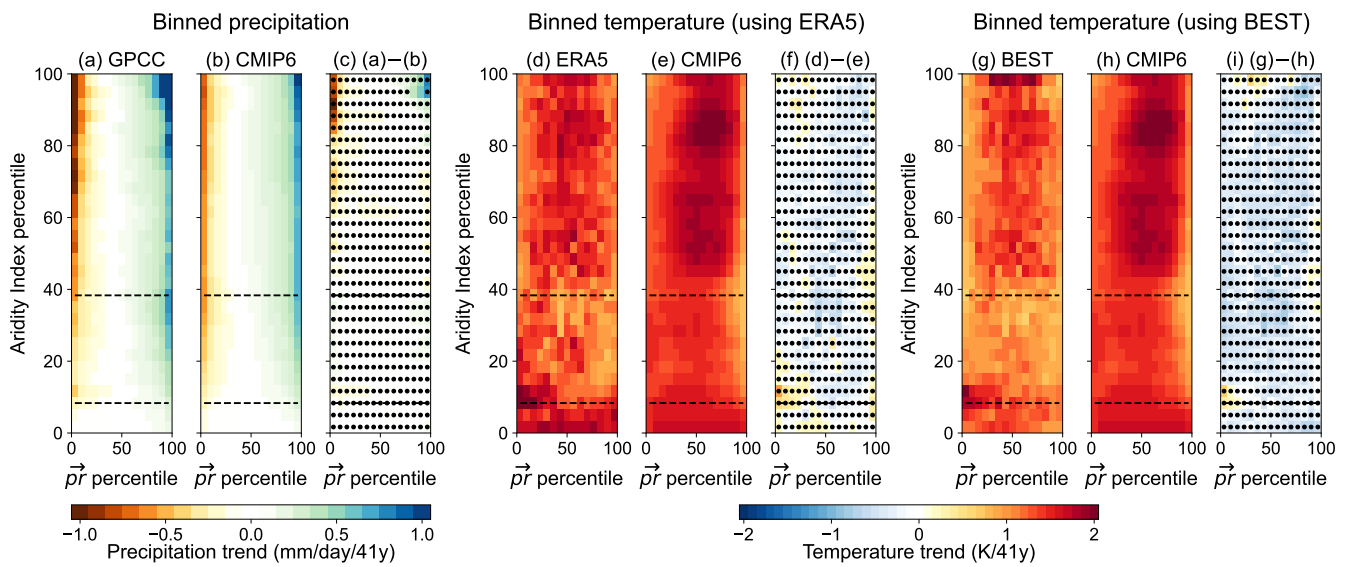
Fig. S14. As Figs 3h-j of the main text but (a)-(c) binning precipitation trends using GPCC, (d)-(f) binning near surface air temperature trends using ERA5, (g)-(i) binning near surface air temperature trends using BEST. All observation-based panels use GPCC precipitation to determine the percentile of precipitation trends.
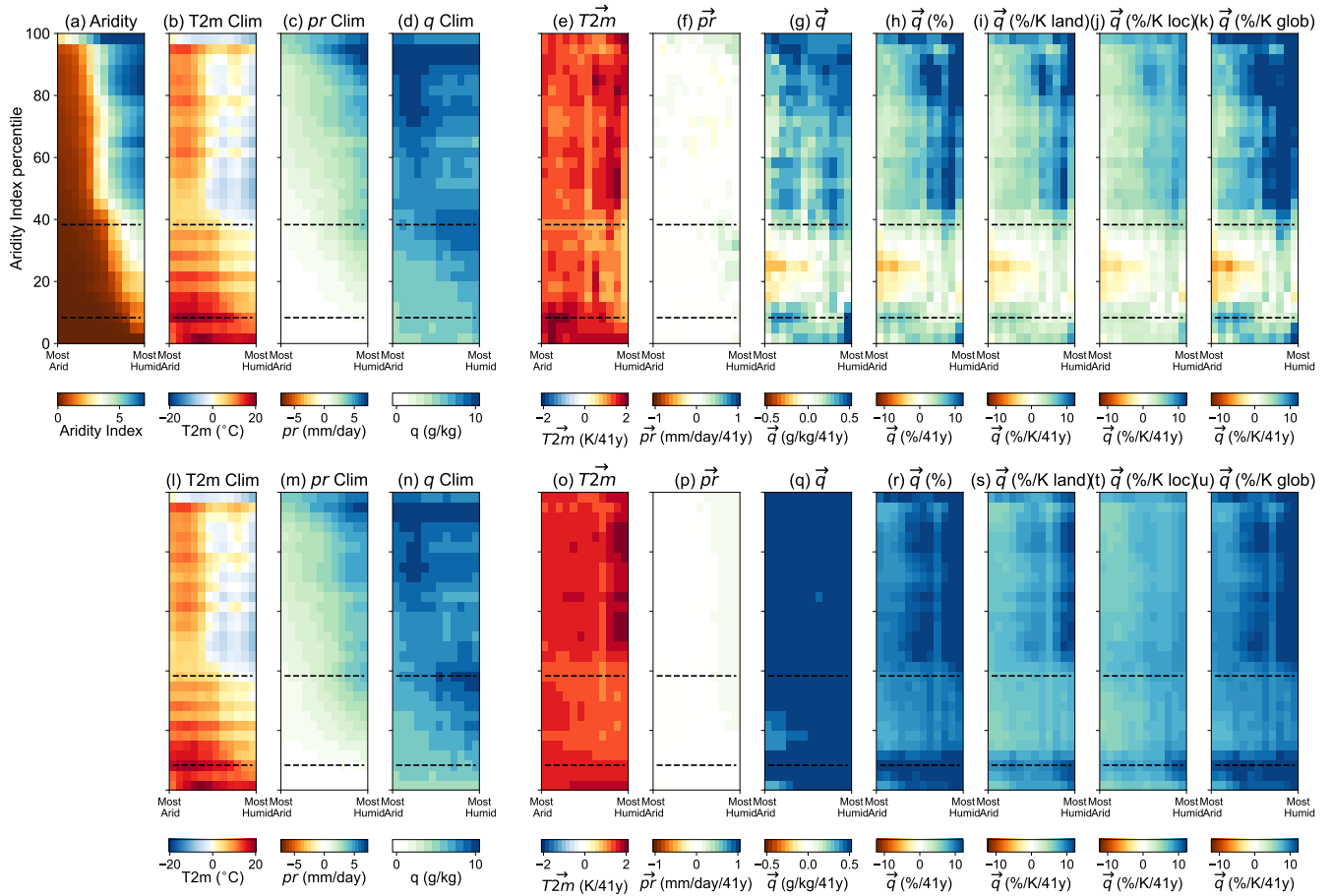
Fig. S15. Complementary plots to those in Fig 3 k to m of the main text of various fields binned according to 30 equal area aridity bins on the y-axis using the observed climatological aridity index, and divided into the 12 months of the year on the x-axis, ordered from the most arid month (with the lowest aridity index) on the left to the most humid month (with the highest aridity index) on the right. The top row shows observation based data and the bottom row shows CMIP6 ensemble means. Panel (a) shows the observation-based aridity index average for each of the bins/months and the remaining panels show: 1980 to 2020 climatological averages of (b)/(l) near surface air temperature, (c)/(m) precipitation, (d)/(n) near surface specific humidity, and 1980 to 2020 trends $\overrightarrow{(.)}$ of (e)/(o) near surface air temperature, (f)/(p) precipitation, (g)/(q) near surface specific humidity, (h)/(r) near surface specific humidity expressed as percentage of the 1980 to 1990 climatology, (i)/(s) are as (h)/(r) but normalized by trends in near surface air temperature averaged over land regions, (j)/(t) are as (h)/(r) but normalizing by local near surface air temperature trends, and (k)/(u) are as (h)/(r) but normalizing by globally averaged near surface air temperature trends.
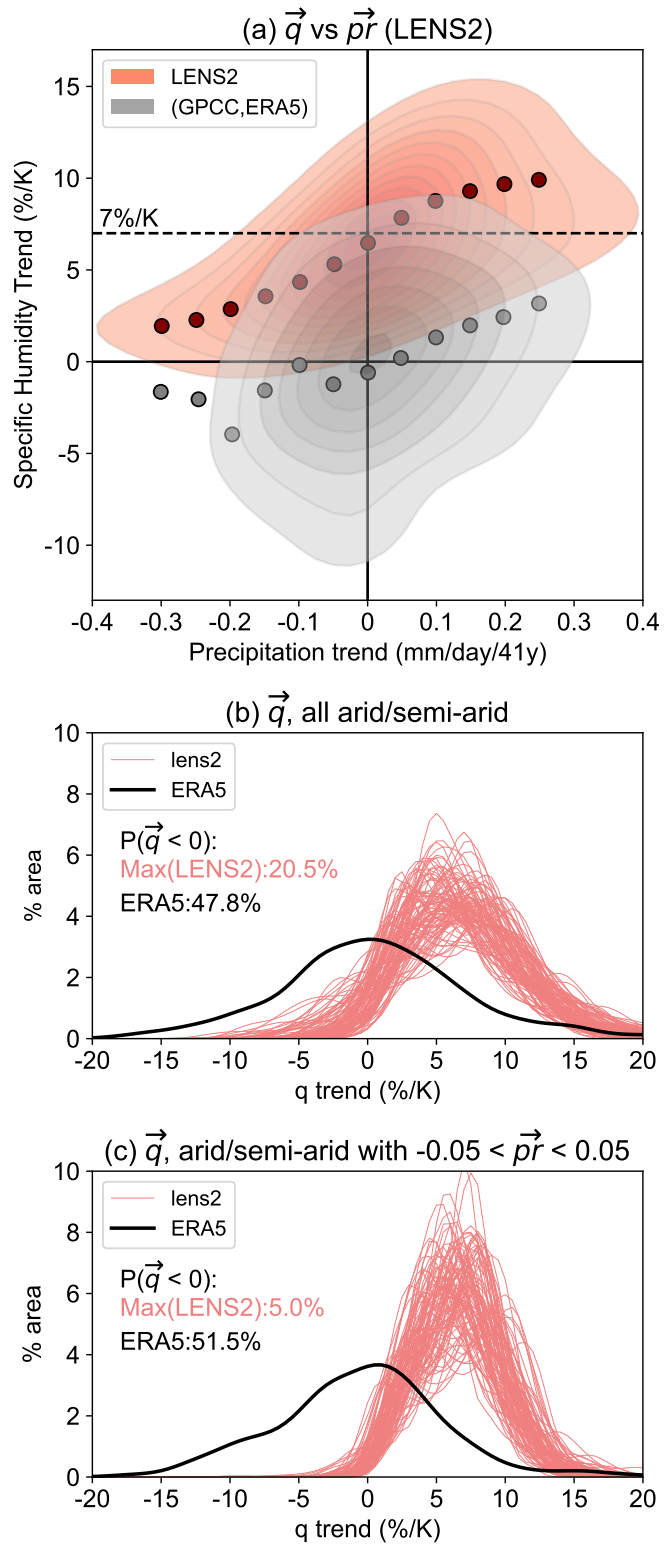
Isla R Simpson, Karen A. McKinnon, Daniel Kennedy, David M. Lawrence, Flavio Lehner, and Richard Seager **19 of 27**

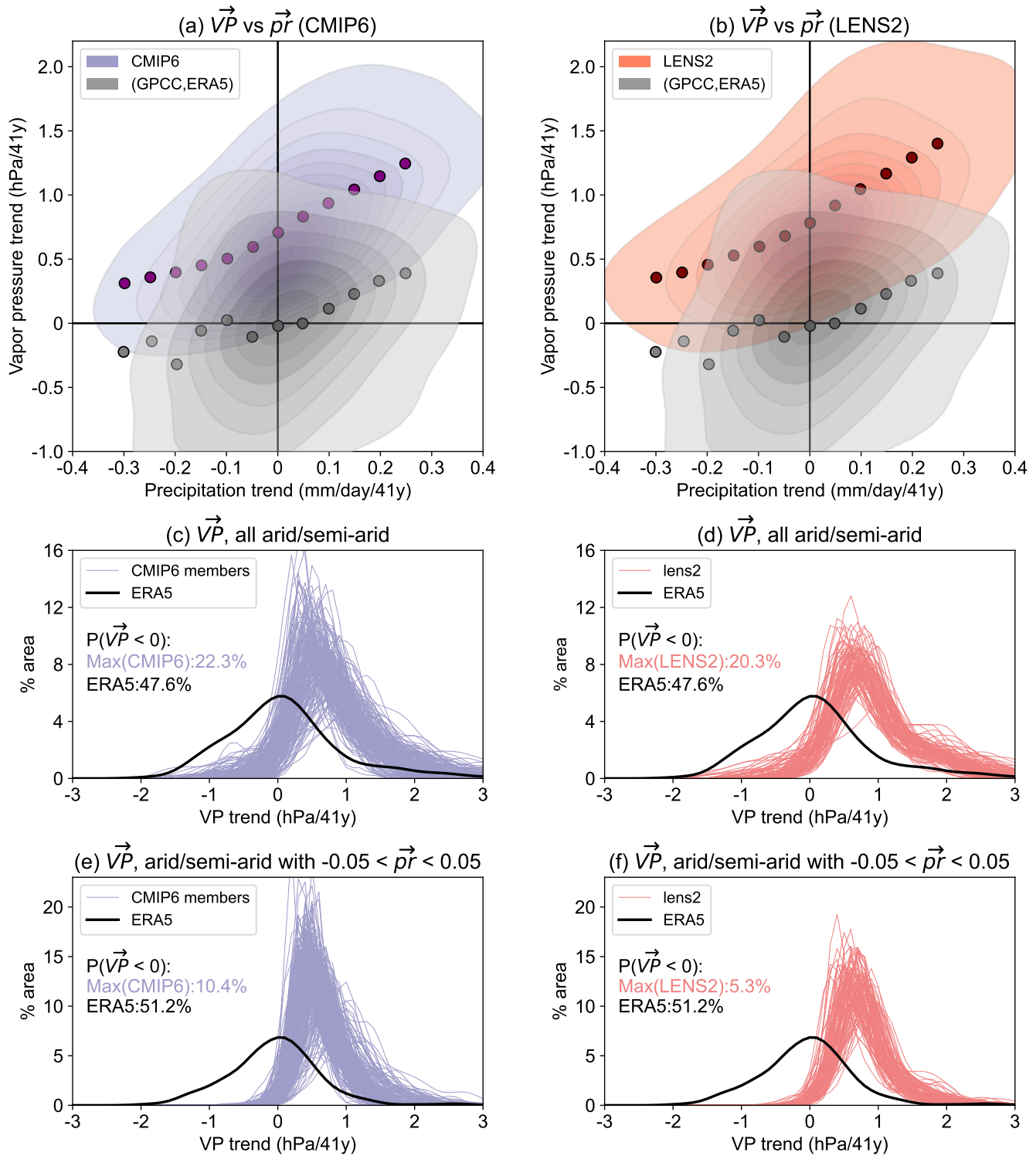**Fig. S16.** As Fig. 4 of the main text but using LENS2.

Fig. S17. As Fig. 4 of the main text and Fig. S16 but using vapor pressure trend ($\overrightarrow{VP}$) and not normalizing by the temperature trend.
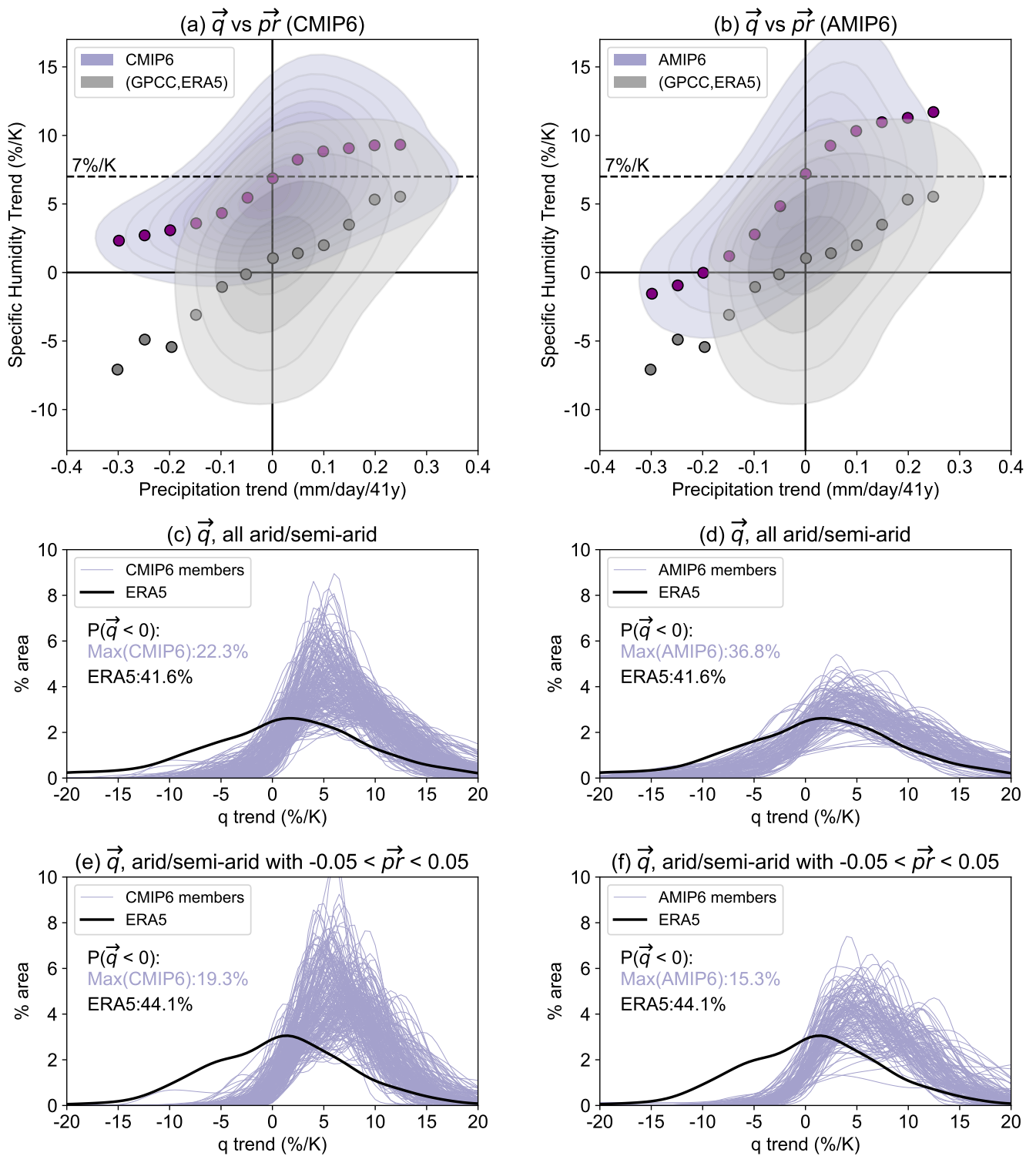
Fig. S18. (left) As Fig 4 of the main text using CMIP6 models but for 1979 to 2014. (right) as (left) but for the AMIP6 simulations.
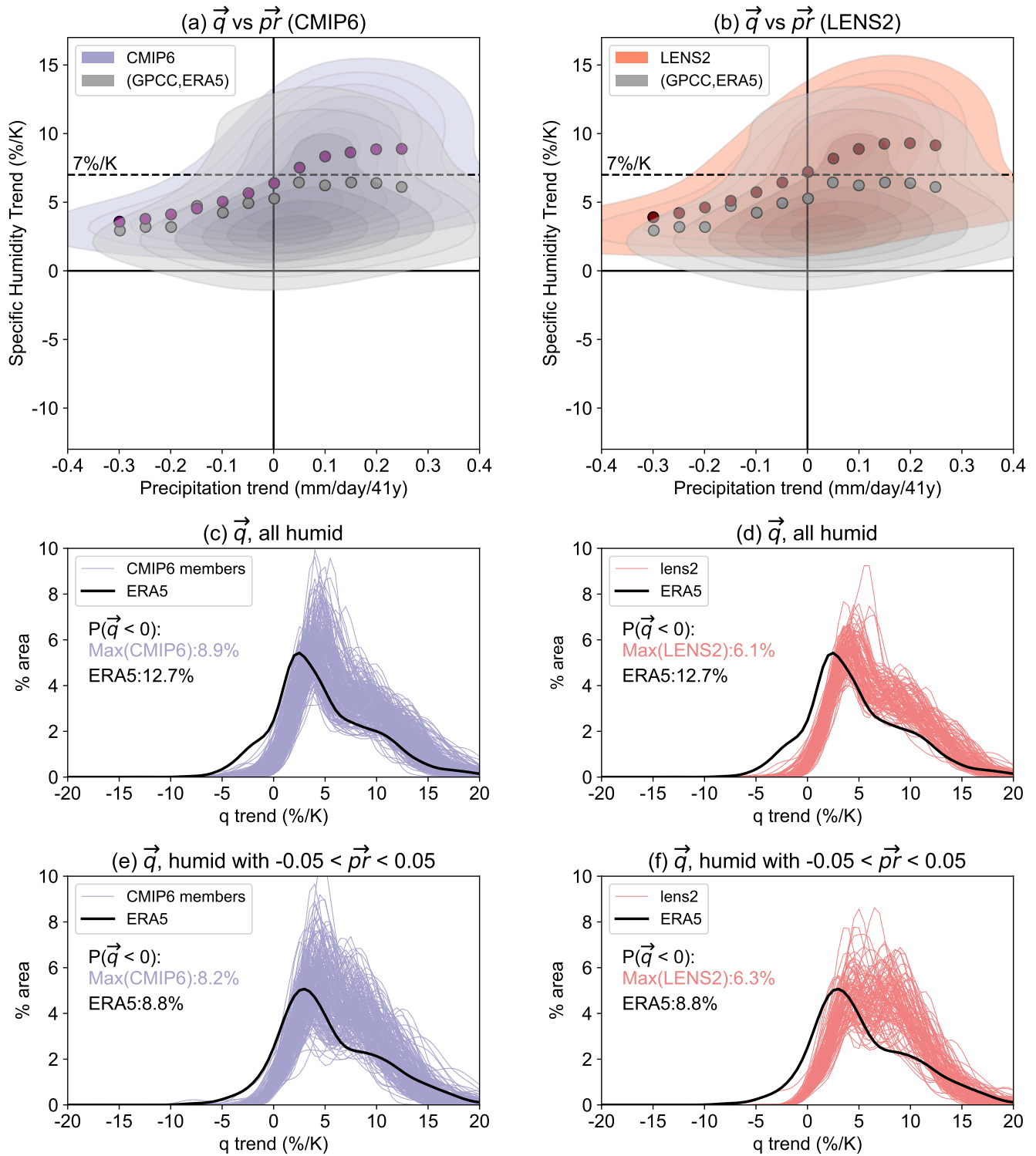
Isla R Simpson, Karen A. McKinnon, Daniel Kennedy, David M. Lawrence, Flavio Lehner, and Richard Seager

Fig. S19. As Fig. 4 of the main text and Fig. S16 but for humid land locations.
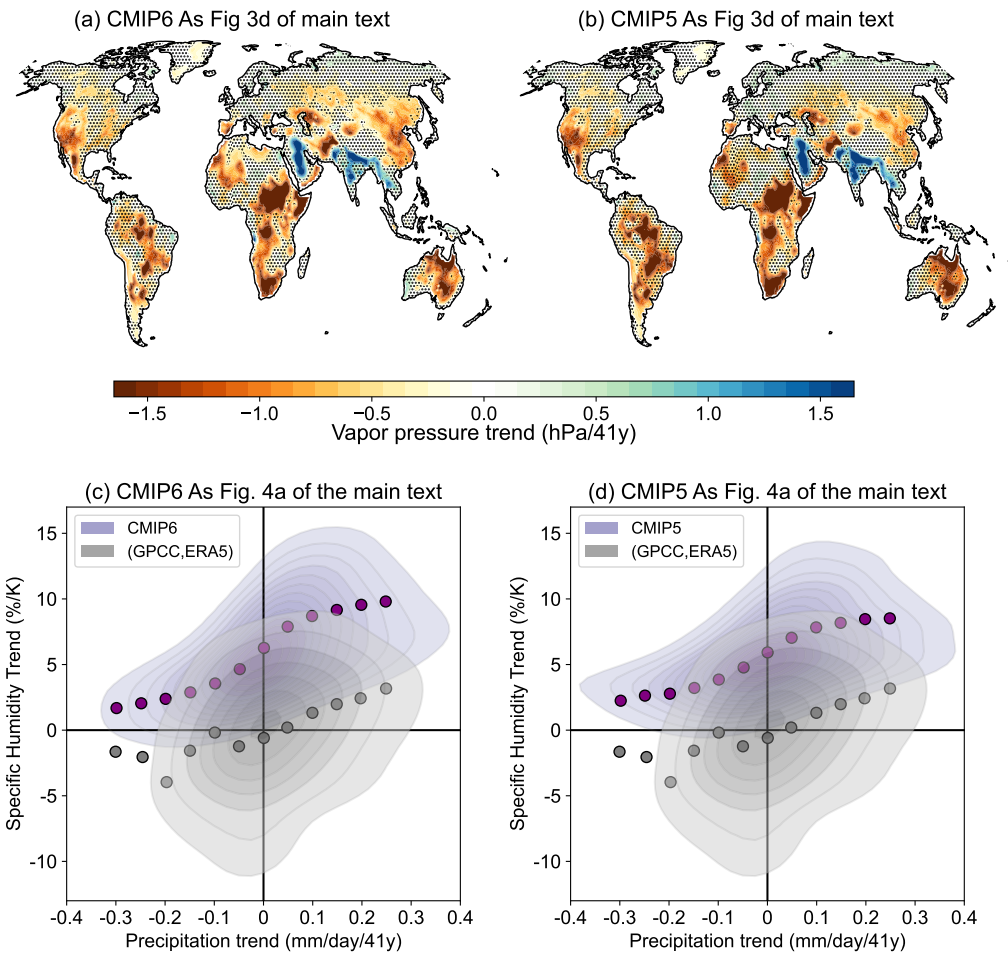
Fig. S20. A comparison of CMIP6 and CMIP5. (a) is the same as Fig. 3d of the main text and (b) is as (a) but using the CMIP5 models. (c) is the same as Fig. 4a of the main text and (d) is the same as (c) but using the CMIP5 models.
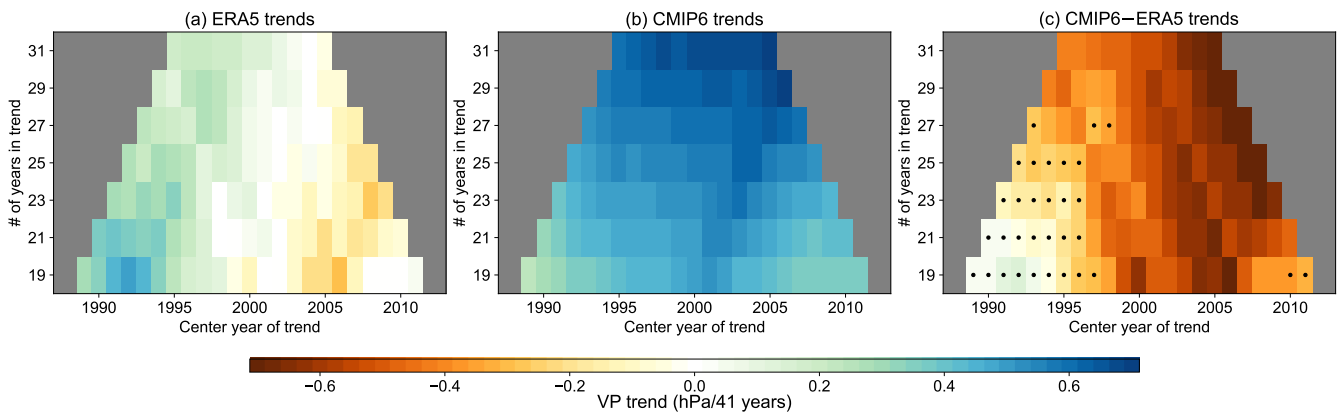
Isla R Simpson, Karen A. McKinnon, Daniel Kennedy, David M. Lawrence, Flavio Lehner, and Richard Seager

Fig. S21. As Fig. S7 but for the area weighted average over arid/semi-arid regions. Rolling trends of the area averaged vapor pressure of length given by the y-axis, centered on the year given by the x-axis. (a) ERA5 trends, (b) ensemble mean of CMIP6 trends, (c) difference between ERA5 and the CMIP6 ensemble mean with dots showing where the ERA5 trend lies within the 2.5th to 97.5th percentile range of CMIP6 ensemble members. Panel (c) indicates a discrepancy in vapor pressure trends between ERA5 and CMIP6 that is robust to trend length and start year except for the earlier shorter trends in the lower left quadrant of the diagram in which the 1997/1998 El Niño year occurs near the end of the trend period in observations, leading to a more positive specific humidity trend (see also Fig. 5c of the main text).
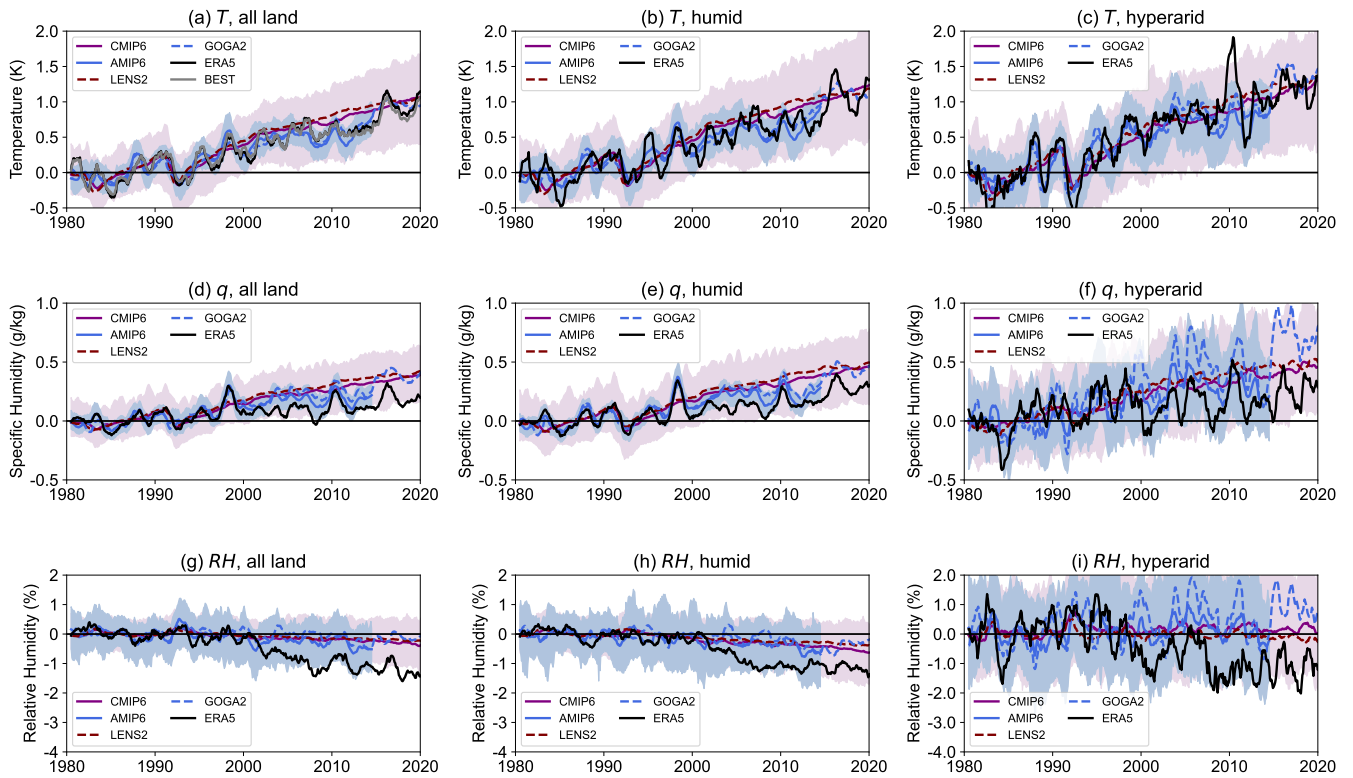
Fig. S22. Area weighted averages of near surface air temperature (top), near surface specific humidity (middle) and near surface relative humidity (bottom). Left shows the average over all land regions, excluding Antarctic, middle shows the average over all humid land regions, and right shows the average over all hyperarid land regions. The thistle colored range shows the 2.5th to 97.5th percentile range across all CMIP6 members from all models, and the blue colored range shows the 2.5th to 97.5th percentile range across all AMIP6 members.
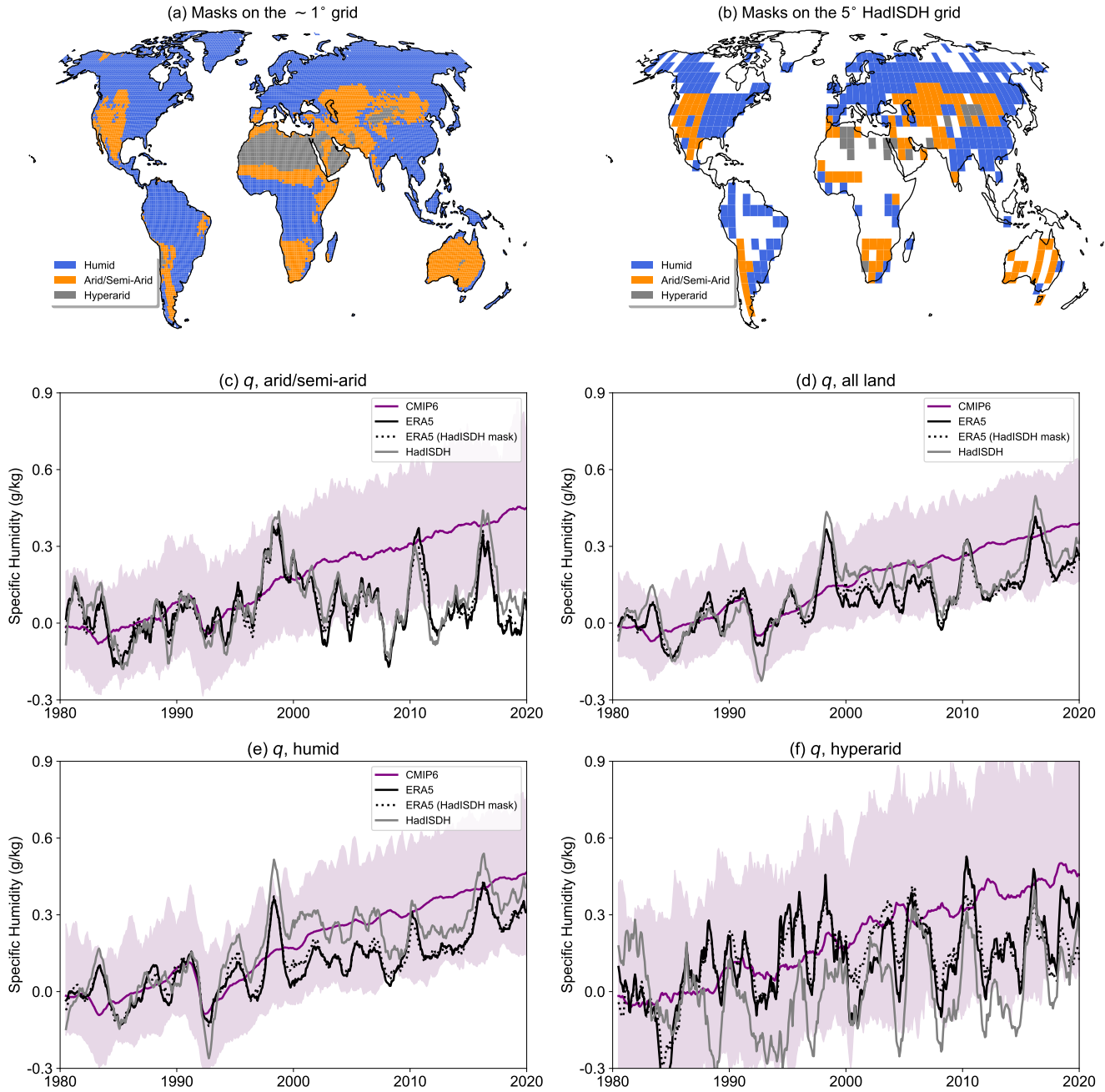
Fig. S23. Comparison of area averaged 12 month running mean time series between ERA5 and the gridded HadISDH dataset. The gridded HadISDH dataset is on a 5° horizontal grid whereas in the main text we have used ERA5 on a 1° grid. HadISDH also has missing locations due to a lack of data availability. Panels (a) and (b) compare the masking regions used for the different aridity zones on the 1° grid of the main text (panel a) and the 5° grid with missing locations (in white) of the gridded HadISDH product (panel b). Panel (c) is equivalent to Fig. 5c of the main text and shows specific humidity averaged over arid and semi-arid regions. Solid black shows ERA5 on the 1 degree grid, which can be compared with ERA5 on the 5° grid with masking equivalent to that in HadISDH (black dotted). Gray shows the area average for HadISDH itself. The conclusions drawn in the main text using ERA5 on the 1° grid without missing locations, holds in the gridded HadISDH product as well. (d)-(f) show the area averages over all land regions (excluding Antarctica), humid regions, and hyperarid regions.

Isla R Simpson, Karen A. McKinnon, Daniel Kennedy, David M. Lawrence, Flavio Lehner, and Richard Seager